Direct evidence of polar nature of ferroelastic twin boundaries in $CaTiO_3$ obtained by second harmonic generation microscope

H. Yokota,[1,*] H. Usami,[1] R. Haumont,[2,3] P. Hicher,[2] J. Kaneshiro,[4] E. K. H. Salje,[5] and Y. Uesu[6,†]

[1]*Department of Physics, Chiba University, 1-33 Yayoi-cho, Inage-ku, Chiba-shi, Chiba 263-8522, Japan*

[2]*Institut de Chimie Moléculaire et Matériaux d'Orsay, Université Paris Sud, 91405 Orsay Cedex, France*

[3]*Laboratoire SPMS, Ecole Centrale Paris, Grande voie des vignes, Chatenay-Malabry, France*

[4]*Quantitative Biology Center, RIKEN, 6-2-3 Furuedai, Suita, Osaka 565-0874, Japan*

[5]*Department of Earth Sciences, Cambridge University, Downing Street, Cambridge CB2 3EQ, United Kingdom*

[6]*Department of Physics, Waseda University, 3-4-1 Okubo, Shinjuku-ku, Tokyo 169-8555, Japan*

(Received 13 March 2014; revised manuscript received 6 April 2014; published 21 April 2014)

The polar nature of twin boundaries (TBs) of inherently nonpolar ferroelastic $CaTiO_3$ is examined by the confocal second harmonic generation (SHG) microscope. Three-dimensional SHG images of samples with the pseudocubic (110) and (1-11) planes confirm that both crystallographically prominent TB (W plane) and nonprominent TB (W' plane) are SHG active and consequently polar. The directions of the electric polarization P_S are determined from the anisotropy of SHG intensities. In the W' plane, the SHG polar diagrams are well fitted using the point-group symmetry 2, which reveals that the P_S directions parallel to the twofold axis do not lie in the W' plane but are tilted from it. In the W plane, the P_S direction lies in the mirror plane of the point-group symmetry m.

DOI: 10.1103/PhysRevB.89.144109 PACS number(s): 77.80.Dj, 77.80.−e, 42.65.Ky

I. INTRODUCTION

Ferroic materials are characterized by the presence of domain structures. The phase with a lower symmetry that appears below the phase transition point is composed of energetically equivalent domains with different orientations [1]. In the case of ferroelectrics, the D-E hysteresis is attributed to the growth of a domain with the polarization direction parallel to the external field, and we can make the analogous statement about ferroelastic materials simply replacing D and E by strain and stress, respectively. The static structure and dynamic behavior of domains have been researched for a long time, and several kinds of applications using domain structures have been developed under the name of domain-engineering [2]. In contrast, domain boundaries did not attract much attention until recently, but in the past five years, their structural, ferroelectric, piezoelectric, conductive nature, as well as defect distributions, have been intensely investigated, in particular, from fundamental viewpoints [3–11]. This field, termed the domain boundary sciences, is becoming increasingly important in nanosciences [12,13].

One of the boundary effects is the ferroelectricity at the twin boundaries (TBs) of ferroelastic materials, which was theoretically predicted prior to the above-mentioned flourishing investigations [14–17]. A similar interface effect was also found in the grain boundaries of $SrTiO_3$ ceramics [18]. The recent growth of this field owes much to the development of new observation technologies that enable us to investigate the structure and physical nature of domain boundaries on an atomic scale. A notable example is a recent work on $CaTiO_3$ (CTO) using the aberration-corrected transmission electron microscopy (TEM), which revealed that the twin boundaries (TBs) of CTO were of a ferroelectric nature with relative displacements of Ti ions at the boundaries [19]. This experimental finding was interpreted using theoretical simulations [19–21]. The works concluded that the polarization direction lies in twin boundary planes of the c domains, and that the magnitude of the spontaneous polarization is comparatively large, though the study was restricted to a special kind of TBs in very thin samples. Another example is the ferroelectric nature of TBs in an STO single crystal, which has been recently disclosed using the resonance piezoelectric spectroscopy [22–24].

The polar nature at the TB of ferroelastic materials can be best explored using observation techniques at different spatial scale, which permit us to determine the symmetry of the TB and the polarization direction of a variety of TBs. The optical second-harmonic generation (SHG) microscope is suitable for this purpose, because, with its large dynamic range of signals, SHG is highly sensitive to changes in P_S [25–28]. Furthermore, when we use the confocal scanning SHG microscope (SHGM), the 3D images of polar structures are available. We developed this type of SHGM operative in the transmission mode [29] and successfully observed periodically poled ferroelectric domain structures in quasiphase matching devices [30,31]. We also analyzed complex domain structures of relaxor and ferroelectric solid solutions at the morphotropic phase boundary to determine the polarization direction and the macroscopic symmetry [32]. Adopting this SHGM, we investigate the polar nature of the TB of CTO in the present study [33].

II. EXPERIMENTAL METHODS

To obtain reliable and reproducible results, we prepared high-quality single crystals using an optical floating-zone furnace CSI FZ-T-4000-H-II-PP (Crystal Systems Corporation, Japan), equipped with four lamps (300 W) installed as infrared radiation sources [34]. The feed rods were prepared

*yokota@physics.s.chiba-u.ac.jp
†uesu93@waseda.jp

by conventional solid-state reactions. Powders of $CaCO_3$ and TiO_2 (purity of 99.95%) were mixed in the nominal molar ratio corresponding to CTO. They were ground in a mortar and precalcined at 1200°C (15 h), then isostatically pressed into a rod, Ø 6 mm × 80 mm, and sintered in air at 1300°C (20 h). The temperature of the molten zone was precisely controlled by adjusting the intensity of the current through the lamps. The crystal growth was carried out in an enclosed quartz tube, where a flow of O_2 was applied. The feed rod and the growing crystal were rotated at 15 rpm in opposite directions to ensure an efficient mixing and uniform temperature distribution in the molten zone. The growth rate was 8 mm/h.

The phase purity and orientation of the resultant crystals were checked by x-ray diffraction. The room temperature diffraction pattern of crushed crystals indicates that single-phase $CaTiO_3$ had been made, free from parasitic impurities. For the SHGM observations, two samples with different orientations were used. Laue photographs, recorded by back-reflection using molybdenum source radiations (0.4 Å $< \lambda <$ 2 Å), confirmed that one sample (CTO-1) has the [110] growth axis and another (CTO-2) has the [1-11] growth axis in the pseudocubic perovskite coordinates. From these x-ray diffraction results, the lattice constants along the orthorhombic axes are determined to be $a_o = 5.445$ Å, $b_o = 5.471$ Å, and $c_o = 7.725$ Å. These values approximately coincide with those obtained by the previous structural study [35]. The samples are cut perpendicular to the growth axis with an orientation error less than 4°. The sample dimensions are 6.6 mm in diameter and 0.50 mm thick for CTO-1 and 3.0 mm in diameter and 0.85 mm thick for CTO-2. The relation between the orthorhombic axes a_o, b_o, c_o, and the pseudocubic axes *a//x*, *b//y*, *c//z* is indicated in Fig. 1. Hereafter the pseudocubic axes are used except on specific notice.

Figure 2 shows the optical setup of the SHGM. An Nd:YVO_4 laser is used as the fundamental wave. Its wavelength is 1064 nm, repetition frequency 40 kHz, pulse width 10 ns, and maximum power of 6 W. The power of fundamental wave is adjusted by an attenuator composed of a half-wave plate and a thin film polarizer. The polarization direction of the fundamental wave is rotated by another half-wave plate. A pair of objectives with a numerical aperture of 0.7 and a pinhole make up the confocal system. The polarization component of the SH wave is selected by an analyzer. Waves with the wavelength of 532 nm are picked up by a spectrometer, and the intensities are detected point by point by a photomultiplier tube, which is synchronized with incident laser pulses by a lock-in amplifier. The sample is moved by a stepping motor along the axial direction and by piezo actuators along the lateral directions. 3D SHG images are constructed by the accumulated SHG intensities. Because the SHG intensities from CTO were extremely weak, less than 10^{-8} times weaker than those of the d_{31} component of $LiNbO_3$, we made a special effort to eliminate stray light that causes background noises.

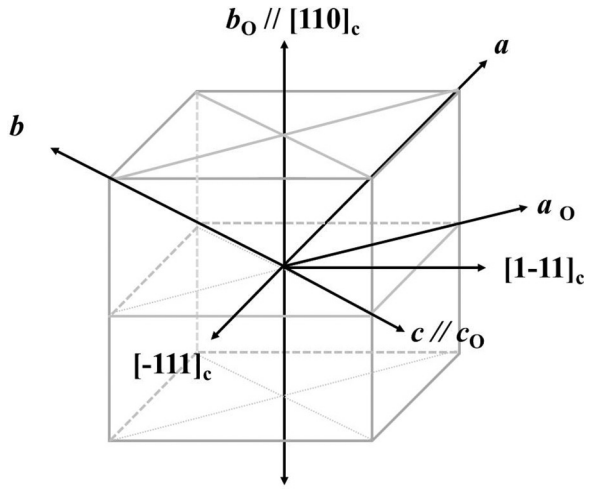

FIG. 1. The relation between the orthorhombic axes a_o, b_o, c_o, and the pseudocubic axes *a//x*, *b//y*, *c//z*. The suffix *O* indicates the orthorhombic coordinate.

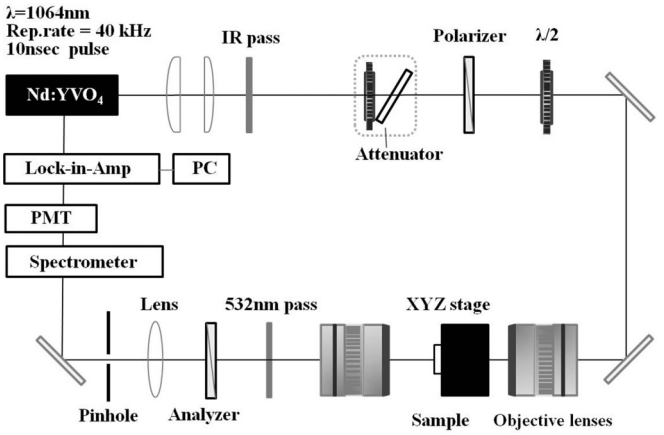

FIG. 2. Optical set-up of the confocal SHG microscope used in the present experiment.

III. SHG MICROSCOPIC OBSERVATIONS AND ANALYSES

A. Results of CTO-1

Figure 3(a) shows a polarization microscope image of the CTO-1 taken in the crossed Nicol configuration. The image reveals fine domains of less than 100 μm in width, most of which are aligned parallel to a specific direction (type A). The image also reveals domains of another type (type B), which are inclined 35° from type A. Clear extinction angles of these domains cannot be determined because TBs are not perpendicular to the sample surface but inclined to it. The type A and B are classified into the W' plane and W planes, respectively [36,37]. The detail analyses are given below.

Subsequently, the same sample is subjected to SHGM observations. Polarization directions of the fundamental and SH waves are fixed parallel to the X axis (see Fig. 3). For 2D scanning, the incident beam is focused on a point slightly below the sample surface to avoid SH waves occasionally produced by the symmetry lowering at the sample surface, which is inevitable even with centrosymmetric crystals. An SHG image of the enclosed region in Fig. 3(a) is shown in Fig. 3(b), which is obtained by 1-μm scanning step in the lateral X-Y plane. It took 20 min. to obtain this 2D image. SHG active lines are observed as bright lines against the dark background. Domains themselves, on the contrary, are dark

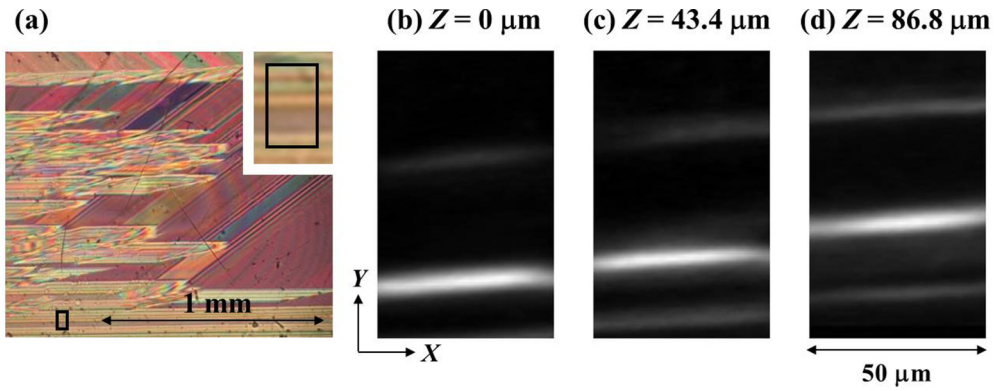

FIG. 3. (Color online) (a) Polarization microscope image of CTO-1 taken in the crossed Nicol configuration. (b–d) SHG section images at different depths (Z) from the surface. The observed area is the enclosed square in (a). A zoom-in picture of the enclosed region is also shown in an inserted figure. Here X and Y axes with capital letters indicate the scanning axes of the SHG microscope, which varied for observation experiments. The coordinate should be discriminated from x, y, z with small letters.

and SHG nonactive. Comparison of the SHG image with the polarization microscopic image makes it clear that SHG-active regions are TBs of ferroelastic domains, which means TBs of ferroelastic CTO are polar. To corroborate the result, we also take SHG pictures using another type of SHGM equipped with a Ti-sapphire laser. Its wavelength is 810 nm, repetition frequency 80 MHz, pulse width 250 fs, and an average power 3.2 W. The sample used in this experiment is also the (110) plate but it is cut out of a different rod synthesized under the same condition as the previous one. The result of this time is identical to the previous one, which irrevocably confirms the polar nature of the TBs in CTO.

To obtain the perspective view of TBs in the sample, cross-section SHG images of the same area as shown in Fig. 3(b) are taken along the [110] axis (Z) at an interval of 43.4 μm. Because the samples of CTO are transparent and no serious absorption problem exists in the present experiment, signal scale and the contrast level for each image are kept constant. The results are shown in Figs. 3(c) and 3(d). The bright lines are observed inside the sample and the assembly of those lines constitutes TB planes, which cut through the sample at an inclination of about 80° to the surface. Figure 4 shows SHG images of another area, where (a)–(c) are the sections (denoted as the X-Y plane) at different Z positions. Two TBs (type A and type B) with different inclinations are observed. Figures 4(d)–4(f) show the Y-Z section images of the same area. As those images show, TBs of type A and type B have inclinations of approximately 80° and 65° from the surface, respectively. The overall TB structure is schematically illustrated in Fig. 4(g). All observable TBs, whether of type A or type B, are SHG active

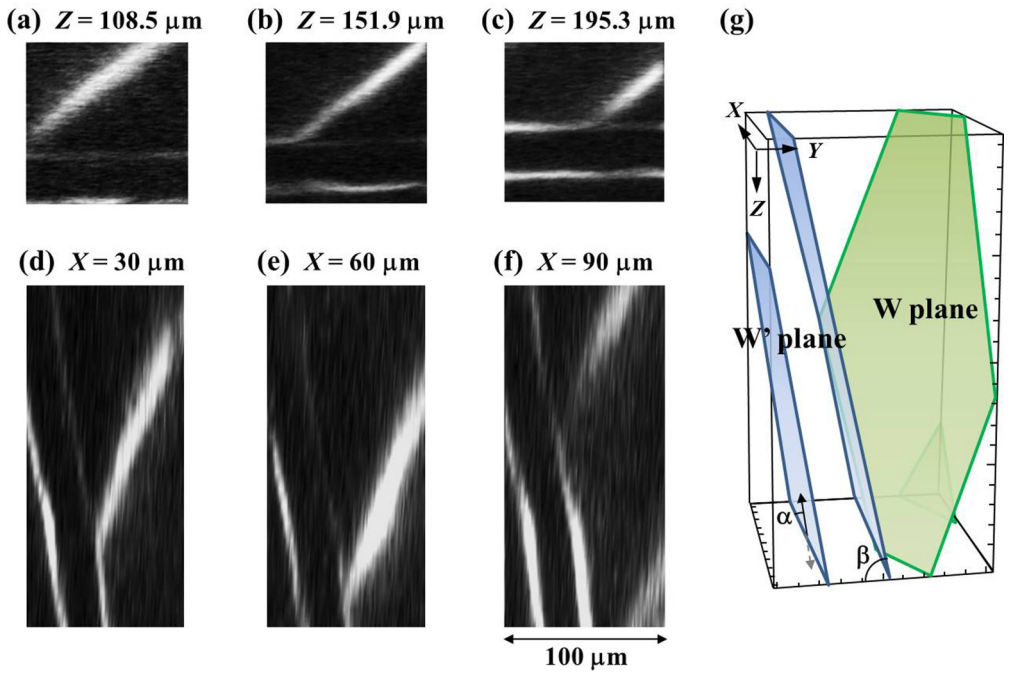

FIG. 4. (Color online) SHG images of another area of CTO-1. (a–c) show the X-Y section images at different Z. (d–f) show the Y-Z section images of the same area. (g) 3D schematic images of TBs of type A (W') and type B (W) in CTO-1.

TABLE I. The type and orientation of the twin boundaries of $CaTiO_3$ looked along the [110] axis. The bold letter columns denote the observed TBs in the present experiments.

Type	Plane equation	Angle between TB and c axis [deg.]	Angle between TB and (110) [deg.]
W-wall	$x = 0$	0	45
	$y = 0$	0	45
	$z = 0$	90	90
	$x = y$	0	90
	$x = -y$	—	—
	$\boldsymbol{y = z}$	**125.3**	**60**
	$\boldsymbol{y = -z}$	**54.7**	**60**
	$\boldsymbol{z = x}$	**54.7**	**60**
	$\boldsymbol{z = -x}$	**125.3**	**60**
W'-wall	$3e_{11}(z+x)+2e_{12}y = 0$	14.6	37.1
	$3e_{11}\,(z+x)-2e_{12}y = 0$	169.2	125.7
	$3e_{11}\,(z-x)+2e_{12}y = 0$	10.8	54.3
	$3e_{11}\,(z-x)-2e_{12}y = 0$	165.4	142.9
	$\boldsymbol{3e_{11}(x+y)+2e_{12}z=0}$	**90**	**77.6**
	$\boldsymbol{3e_{11}(x+y)-2e_{12}z=0}$	**90**	**77.6**
	$3e_{11}\,(y-x)+2e_{12}z = 0$	77.6	90
	$3e_{11}\,(y-x)-2e_{12}z = 0$	102.4	90
	$3e_{11}\,(y+z)+2e_{12}x = 0$	14.6	37.1
	$3e_{11}\,(y+z)-2e_{12}x = 0$	169.2	125.7
	$3e_{11}\,(y-z)+2e_{12}x = 0$	14.6	37.1
	$3e_{11}\,(y-z)-2e_{12}x = 0$	169.2	125.7

and polar. In the vicinity of the region where the two types of TBs intersect, the SH intensity increases. This is probably because a lattice strain becomes larger due to the increase of an elastic energy near the intersection region of different domains. It would enhance the polarization through the piezoelectric effect and eventually the SH intensity increases. It may give some hints for future applications of the domain boundary engineering. The TB in this region is bent and the inclination angle changes as shown in Fig. 4(f), which is considered to release large strain energy, but an extra strain could still remain.

The orientations of type A and B are expressed by Eqs. (1) and (2), respectively, which are derived by the strain compatibility theory concerning $m\bar{3}mFmmm$ ferroelastic phase transition accompanied by a 45° rotation around the c axis [36].

$$3e_{11}(x+y) \pm 2e_{12}z = 0, \tag{1}$$

$$y = \pm z \text{ or } z = \pm x. \tag{2}$$

Here, spontaneous strains e_{11} ($=e_{22}$) and e_{12} are referred to be the pseudocubic axes and expressed by the following matrix:

$$\begin{pmatrix} e_{11} & e_{12} & 0 \\ e_{12} & e_{11} & 0 \\ 0 & 0 & -2e_{11} \end{pmatrix}.$$

For CTO, e_{11} and e_{12} are calculated from the lattice constants at room temperature determined by XRD measurements [38]. We then obtain $e_{11} = 5.7 \times 10^{-4}$ and $e_{12} = 5.5 \times 10^{-3}$, which explains the present experimental results within the experimental errors [39].

According to the theory, there exist 21 TBs, of which 9 TBs are crystallographically prominent W planes and the remaining 12 TBs crystallographically nonprominent W' planes. The type (W or W'), the plane equation, and the angle between the TB and the [001] axis and the angle between the TB and the (110) plane are tabulated in Table I. The W planes are all mirror planes, while the orientations of the W' planes depend on the lattice constants and each of the W' planes contains one twofold axis perpendicular to the paired W plane. Therefore, the type A plane is a W' plane and the type B plane a W plane. This fact is used for analyzing the anisotropy of SHG intensities at TBs.

The anisotropy of SHG intensities in the TBs is measured to determine the symmetry and the polar directions of the TBs. The polarization directions of the fundamental wave and that of SH wave are kept parallel to each other and rotated together. The 2D distribution of the SHG intensities is mapped on an array of polar diagrams by dividing a square area of 100 × 100 μm^2 into cells in the X-Y plane. Figure 5(a) shows the SHG image of an area that contains three SHG active TBs of type A. The corresponding polar diagrams mapping is shown in Fig. 5(b). Each of type A TBs exhibits a two-wing diagram with the twofold symmetry of almost the same pattern. Three of those TBs, however, had their principal axes in different directions from that of the others; TB3 has its principal axis almost parallel to the TB line, and TB1 and TB2 have theirs tilted in the opposite directions. We attempt to fit these polar diagrams using Eqs. (3)–(7) on the assumption that the twofold axis lies in the W' plane with the tilting angle α from the normal to the paired W plane (x-y plane).

$$I^{(2\omega)} \propto P^2 = [(-P_1\sin\alpha + P_2\cos\alpha)\cos\theta + (-P_1\cos\alpha\cos\beta - P_2\sin\alpha\cos\beta + P_3\sin\beta)\sin\theta]^2, \tag{3}$$

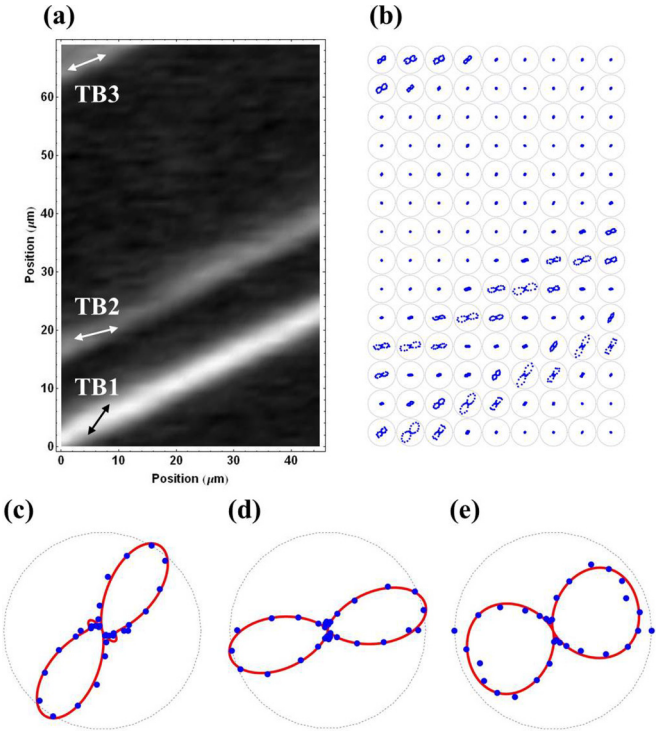

FIG. 5. (Color online) (a) SHG image of an area that contains three SHG active TBs of type A. The corresponding polar diagrams mapping is shown in (b). (c–e) Fitting results for TB1, TB2, and TB3, respectively.

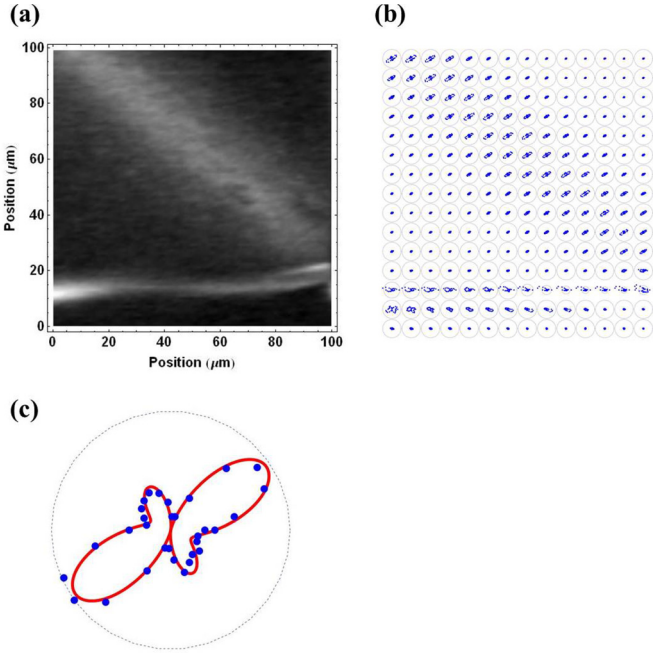

FIG. 6. (Color online) (a) and (b) SHG image and the corresponding polar diagrams mapping of type B, respectively. The fitting result is indicated in (c).

$$\begin{aligned} P_1 &\propto \chi_{14}E_2E_3 + \chi_{21}E_1E_2 \\ P_2 &\propto \chi_{21}E_1^2 + \chi_{22}E_2^2 + \chi_{23}E_3^2 + \chi_{14}E_1E_3 \\ P_3 &\propto \chi_{23}E_2E_3 + \chi_{14}E_1E_2, \end{aligned} \tag{4}$$

$$\begin{aligned} E_1 &= -E_0\cos\theta\sin\alpha - E_0\sin\theta\cos\alpha\cos\beta \\ E_2 &= E_0\cos\theta\cos\alpha + E_0\sin\theta\sin\alpha\cos\beta \\ E_3 &= E_0\sin\theta\sin\beta, \end{aligned} \tag{5}$$

where

$$\chi_{il} = d_{il}/\Delta k(ij), \tag{6}$$

with

$$\Delta k = 4\pi(n^{(2\omega)} - n^{(\omega)})/\lambda. \tag{7}$$

In the above equations, θ is the rotation angle of the coupled polarizer and analyzer from the X axis and β is the inclination (=80°) of W' plane. The d_{ij} ($i = 1 \sim 3$, $j = 1 \sim 6$) in Eq. (6) is the SHG tensor component in the Voigt notation [40]. The Kleiman symmetry conditions for d constants are adopted [41]. The λ in Eq. (7) denotes the wavelength of the fundamental wave, and $n^{(\omega)}$ and $n^{(2\omega)}$ are the refractive indices of the fundamental and SH waves, respectively. The results are shown in Figs. 5(c)–5(e) for TB1, TB2, and TB3, respectively. The tilting angles from the TB lines are determined to be ±30°. This result indicates that the P_S of TB1 and that of TB2 are tilted in the opposite directions in the adjacent TB planes. This tilting is apparently contradictory to the anticipation that the twofold axis would be perpendicular to the paired W plane [36]. This issue will be discussed in the next paragraph.

The SHG image and the corresponding SHG polar diagram mapping of W plane (type B) are shown in Figs. 6(a) and 6(b), respectively. The P_S lies in the mirror plane. The polar diagram fitting follows a similar but modified procedure as in the case of W' plane with $\alpha = 0$ and $\beta = 65°$.

$$\begin{aligned} I^{(2\omega)} \propto P^2 = \Bigg[\left\{ \frac{1}{\sqrt{2}}P_1 + \frac{1}{\sqrt{3}}P_2 + \frac{1}{\sqrt{6}}P_3\cos\alpha \right\}\cos\theta \\ + \frac{1}{\sqrt{3}}(-P_2 + P_3)\sin\theta \Bigg]^2, \end{aligned} \tag{8}$$

$$\begin{aligned} P_1 &\propto \chi_{11}E_1^2 + \chi_{12}E_2^2 + \chi_{13}E_3^2 + \chi_{15}E_1E_3 \\ P_2 &\propto \chi_{24}E_2E_3 + \chi_{12}E_1E_2 \\ P_3 &\propto \chi_{15}E_1^2 + \chi_{24}E_2^2 + \chi_{33}E_3^2 + \chi_{13}E_3E_1, \end{aligned} \tag{9}$$

$$\begin{aligned} E_1 &= \frac{1}{\sqrt{2}}\cos\theta \\ E_2 &= \frac{1}{\sqrt{3}}\cos\theta - \frac{1}{\sqrt{3}}\sin\theta \\ E_3 &= \frac{1}{\sqrt{6}}\cos\alpha\cos\theta + \frac{1}{\sqrt{3}}\cos\alpha\sin\theta. \end{aligned} \tag{10}$$

The result is shown in Fig. 6(c). The coincidence between the experiment and calculation is satisfactory also in this case.

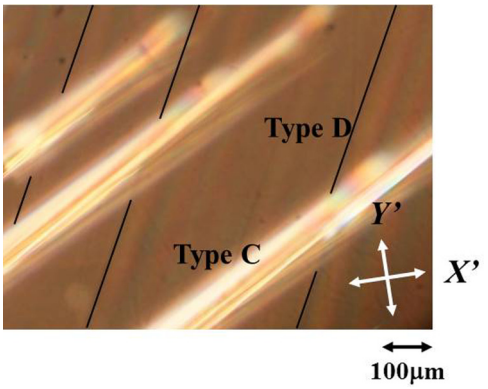

FIG. 7. (Color online) The polarization microscope image of CTO-2 taken in the crossed Nicol configuration. White cross (X' and Y' axes) indicates the extinction angle of the area where type D is observed. The black lines are added for making clear the locations of TBs. Three bright regions correspond to type C. Arrows in Fig. 5(a) show the projection of the electric polarization onto the section plane.

B. The results of CTO-2

The twin structure of CTO-2 is simpler than those of CTO-1 as shown in Fig. 7, which is a polarization microscope image. There exist two types of twin structures, type C and type D, both of which cannot be distinguished by the extinction position. Figures 8(a) and 8(b) show the corresponding SHGM section images of type C in the *X*-*Y* plane perpendicular to the [1-11] axis, and Fig. 8(c) shows the *Z*-*X* image of type C. Figures 9(a) and 9(b) are those of type D. These TBs are all SHG active and polar as in CTO-1. These 3D-SHG images reveal that TB1 is almost perpendicular to the (1-11) plane. The inclination of type D can be determined form the *X*-*Z* section image shown in Fig. 9(c) and it is approximately 64.5°. The SHG intensity distribution in the type D is fairly broad in comparison with the type C, because the TB is inclined and the area within the focal depth becomes larger. The type and orientation of the TBs are determined by analyzing 3D SHG images with the help of the strain compatibility of TBs and strains e_{11} and e_{12} of CTO, and the results are shown in Table II with all other possible TBs in CTO looked along the [1-11] axis. The type C is probed to be W, while type D is W', and these two types of TBs are shown in bold letters in this table. It should be noted that there exist two possible combinations of the plane equations, i.e., $z = x$, $3e_{11}(y\text{-}z) + 2e_{12}x = 0$ or $y = -z$, $3e_{11}(z + x) + 2e_{12}y = 0$, to explain the experimental results.

IV. DISCUSSION AND CONCLUSION

A. Characteristics of the polar nature of $CaTiO_3$ obtained from the SHGM observations

Here we discuss the characteristics of the polar nature of CTO obtained by the present studies, comparing the previous works on CTO and STO.

The present study reveals that both W and W' TBs of CTO belong to the polar point group m and 2, respectively [42]. This new finding owes to the 3D and nondestructive observations that can be realized by the confocal SHGM. The result agrees with the TEM observations, though the TEM

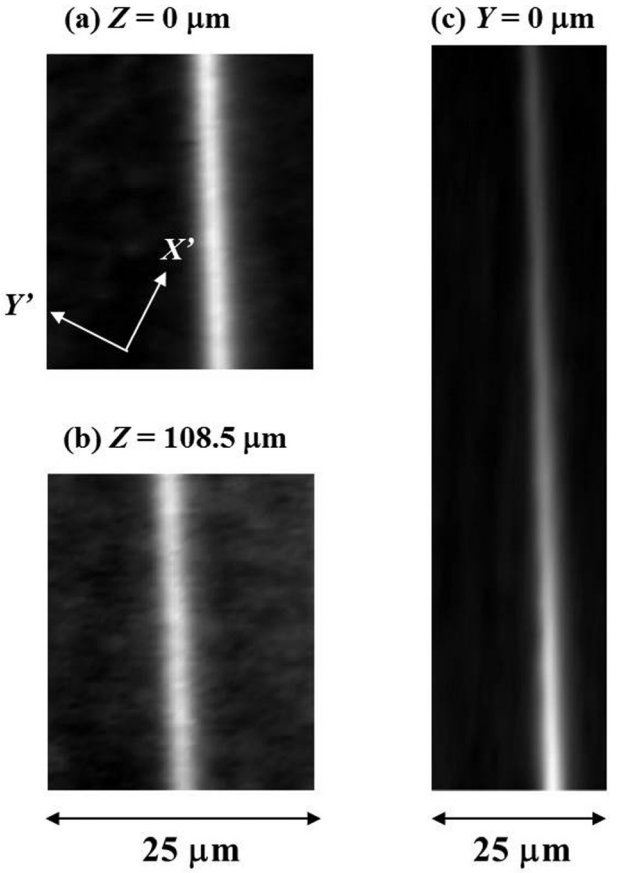

FIG. 8. (a) and (b) SHG *X*-*Y* section images of type C in CTO-2 with different depths (Z) along the [1-11] axis, and (c) shows to the *X*-*Z* section image of the same area.

observation revealed one kind of TBs, likely the W-type TB [19]. The two polar symmetries, 2 and m, of the TBs in CTO coincide with the results obtained by the strain compatibility theory, one applicable to the 3D TBs [36] and another to the layer TBs [16]. However, these theories cannot explain the fact that the direction of the polar axis of W'-type TB is not in the

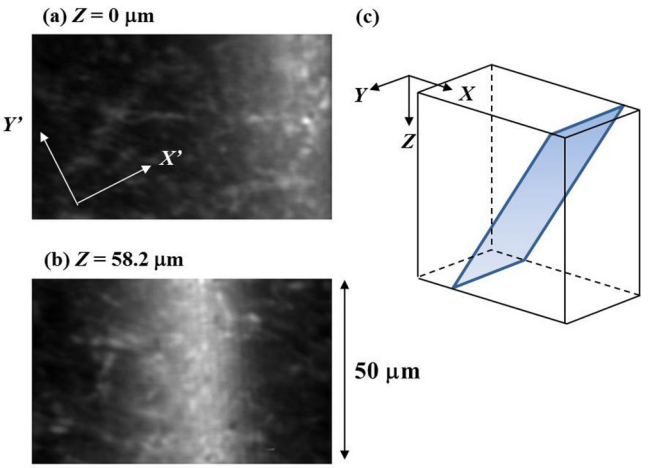

FIG. 9. (Color online) (a) and (b) SHG *X*-*Y* section SHG image of type D in CTO-2 with different Z. (c) Schematic 3D image of type D.

TABLE II. The type and orientation of the twin boundaries of $CaTiO_3$ looked along the [1-11] axis. The bold letter columns denote the observed TBs in the present experiments.

Type	Plane equation	Angle between TB and [110] axis [deg.]	Angle between TB and (1-11) plane [deg.]
W-wall	$x = 0$	60	54.7
	$y = 0$	60	54.7
	$z = 0$	0	54.7
	$x = y$	0	35.3
	$x = -y$	90	90
	$y = z$	60	144.7
	$\boldsymbol{y = -z}$	**150**	**90**
	$\boldsymbol{z = x}$	**30**	**90**
	$z = -x$	60	35.3
W' wall	$\boldsymbol{3e_{11}(z+x)+2e_{12}y=0}$	**60**	**112.9**
	$3e_{11}\,(z+x)-2e_{12}y=0$	60	42.3
	$3e_{11}\,(z-x)+2e_{12}y=0$	44.9	124.3
	$3e_{11}\,(z-x)-2e_{12}y=0$	104.9	55.7
	$3e_{11}\,(x+y)+2e_{12}z=0$	15.1	55.7
	$3e_{11}\,(x+y)-2e_{12}z=0$	15.1	124.3
	$3e_{11}\,(y-x)+2e_{12}z=0$	0	67.1
	$3e_{11}\,(y-x)-2e_{12}z=0$	0	137.7
	$3e_{11}\,(y+z)+2e_{12}x=0$	75.1	55.7
	$3e_{11}\,(y+z)-2e_{12}x=0$	44.9	124.3
	$\boldsymbol{3e_{11}(y-z)+2e_{12}x=0}$	**60**	**67.1**
	$3e_{11}\,(y-z)-2e_{12}x=0$	60	137.7

TB plane but is inclined toward its normal. These inclination angles are opposite to adjacent TBs with a comparatively short distance between the neighbors. On the contrary, the polar axis is located in the TB plane, when the TB plane is wide apart from its neighbors. This fact seems to be indicating the importance of the interaction between TBs, which are not taken into account in the above-mentioned theories. It is, however, just a speculation and further theoretical and experimental works are requested. On the other hand, the previous work pointed out that the TBs have two components of the electric polarization, one is parallel and another is perpendicular to the TB plane [19]. Probably the polar senses of these nearly located TBs are opposite as observed by TEM, and this expectation can be proved if we use the interference SHGM system [29,30], though it is challenging because of extremely weak SHG intensities from TBs.

The origin of the ferroelectric nature at TBs in ferroelastics was explained as a result of shifts of Ti ions toward the specific apex of the oxygen octahedra at TB, which is consequent on nontilted octahedral [19,20]. This phenomenon was also discussed in terms of the flexoelectricity, i.e., the strain-gradient-induced effect on $SrTiO_3$(STO) using the Ginzburg-Landau-Devonshire free energy [20,43]. In particular, Ref. [43] claims that the polarization and pyroelectric response appear across TB and antiphase boundaries in certain temperature ranges below the ferrodistortive phase transition. This approach is substantially equivalent to the previous one introducing the Houchmandazeh-Laizerowicz-Salje (HLS) coupling term $\lambda Q^2 P^2$ ($\lambda > 0$) [16]. Although there exists discussions on the possible application of these continuum theories to the atomic scale phenomenon occurring at TBs, these theories may give some indication on the inclination of the polar axis at TBs observed in CTO.

The polar nature of the TBs in STO has been recently confirmed by the resonance piezoelectric spectroscopy [22–24]. TBs are different in kind for CTO and STO, because the ferroelastic phase transitions take place in different manners accompanying the oxygen octahedral tilts of $a^+b^+c^-$ in CTO and $a^0b^0c^-$ in STO expressed with the Glazer notation [44]. As a result, a more complex picture can be drawn on the polar nature of the interfaces of CTO accompanying all components of tilting vector and polarization vector along the x, y, and z axes.

B. On some issues of the SHG microscope

SHG microscopic observations have two inherent issues to consider, one regarding the visibility inside the samples and the other the spatial resolution of the SHGM we use. As for the first issue, we pointed out in another report that the visibility depends strongly on the sign of the wave-number misfit Δk and that clear SHG images from the inside can be obtained when Δk is negative [30]. In the case of CTO, however, although exact values of the anisotropy and wavelength dispersion of refractive indices are not known and Δk has to be estimated, clear SHG images of the TBs can be observed even when the estimated Δk is positive. This is because SHG-active TBs sharply contrast with dark SHG-inactive domains. The second issue arises from the microscopy we use. It is a far-field optical microscope, and the spatial resolution is restricted by the optical diffraction limit, which is about 0.5 μm along the lateral direction and 4 μm along the axial direction. As a result, the line width observed with our SHGM is not the true TB width but the convolution of the resolution function of the SHGM and the true TB width. According to the atomic scale observations using an aberration-corrected TEM, the width of

the (110)-type TB (W) of CTO was about two octahedra, ~1 nm [19]. The fact that the SHG signal can be detected from such a thin line indicates that the TBs generate large P_S, as was estimated in the report.

In conclusion, we successfully adopted the SHG microscope to confirm the polar nature of the ferroelastic twin boundaries in $CaTiO_3$. We ascertained for the first time that, like the W planes, W' planes are also SHG active and consequently of polar nature. The electric polarization directions were found tilted at different angles for different TBs.

ACKNOWLEDGMENTS

H.Y. acknowledges the support by Grant-in-Aid for Young Scientists (B), and Y.U. acknowledges the support by Grant-in-Aid for Scientific Research (C) from the Ministry of Education, Culture, Sports, Science and Technology, Japan. The authors are grateful to Dr. M. Madono for his critical reading of the manuscript and to Dr. T. M. Watanabe for providing the opportunity to use an SHG microscope at RIKEN to confirm the result obtained by the SHG microscope at Chiba Univ.

[1] E. K. H. Salje, *Phase Transitions in Ferroelastic and Co-Elastic Crystals* (Cambridge University Press, Cambridge, UK, 1993).
[2] For example, M. M. Fejer, G. A. Magel, D. H. Jundt, and R. L. Byer, IEEE J. Quantum Electron. **28**, 2631 (1992).
[3] W. T. Lee, E. K. H. Salje, and U. Bismayer, Phys. Rev. B **72**, 104116 (2005).
[4] L. Goncalves-Ferreira, S. A. T. Redfern, E. Artacho, E. K. H. Salje, and W. T. Lee, Phys. Rev. B **81**, 024109 (2010).
[5] Y. Kim, M. Alexe, and E. K. H. Salje, Appl. Phys. Lett. **96**, 032904 (2010).
[6] J. Seidel, P. Maksymovych, Y. Batra, A. Katan, S.-Y. Yang, Q. He, A. P. Baddorf, S. V. Kalinin, C.-H. Yang, J.-C. Yang, Y.-H. Chu, E. K. H. Salje, H. Wormeester, M. Salmeron, and R. Ramesh, Phys. Rev. Lett. **105**, 197603 (2010).
[7] A. Y. Borisevich *et al.*, ACS Nano **4**, 6071 (2010).
[8] T. Sluka, A. K. Tagantsev, P. Bednyakov, and N. Setter, Nature Commun. **4**, 2839 (2013).
[9] S. Y. Yang, J. Seidel, S. J. Byrnes, P. Shafer, C.-H. Yang, M. D. Rossell, P. Yu, Y.-H. Chu, J. F. Scott, J. W. Ager, III, L. W. Martin, and R. Ramesh, Nature Nanotechnol. **5**, 143 (2010).
[10] A. Lubk, S. Gemming, and N. A. Spaldin, Phys. Rev. B **80**, 104110 (2009).
[11] T. Sluka, A. K. Tagantsev, D. Damjanovic, M. Gureev, and N. Setter, Nature Commun. **3**, 748 (2012).
[12] E. K. H. Salje and H. L. Zhang. Phase Transitions **82**, 452 (2009).
[13] G. Catalan, J. Seidel, R. Ramesh, and J. F. Scott, Rev. Mod. Phys. **84**, 119 (2012).
[14] B. Houchmandzadeh, J. Lajzerowicz, and E. K. H. Salje, J. Phys. Condens. Matter **4**, 9779 (1992).
[15] B. Houchmandzadeh, J. Lajzerowicz, and E. K. H. Salje, J. Phys. Condens. Matter **3**, 5163 (1991).
[16] V. Janovec, L. Richterova, and J. Privratska, Ferroelectrics **222**, 73 (1999).
[17] A. K. Tagantsev, E. Courtens, and L. Arzel, Phys. Rev. B **64**, 224107 (2001).
[18] J. Petzelt *et al.*, Phys. Rev. B **64**, 184111 (2001).
[19] S. Van Aert, S. Turner, R. Delville, D. Schryvers, G. Van Tendeloo, and E. K. H. Salje. Adv. Materials **24**, 523 (2012).
[20] L. Goncalves-Ferreira, S. A. T. Redfern, E. Artacho, and E. K. H. Salje, Phys. Rev. Lett. **101**, 097602 (2008).
[21] L. Goncalves-Ferreira, S. A. T. Redfern, E. Artacho, and E. K. H. Salje, Appl. Phys. Lett. **94**, 081903 (2009).
[22] P. Zubko, G. Catalan, A. Buckley, P. R. L. Welche, and J. F. Scott, Phys. Rev. Lett. **99**, 167601 (2007).
[23] J. F. Scott, E. K. H. Salje, and M. A. Carpenter, Phys. Rev. Lett. **109**, 187601 (2012).
[24] E. K. H. Salje, O. Aktas, M. A. Carpenter, V. V. Laguta, and J. F. Scott, Phys. Rev. Lett. **111**, 247603 (2013).
[25] E. D. Mishina, N. E. Sherstyuk, D. R. Barskiy, A. S. Sigov, Yu. I. Golovko, V. M. Mukhorotov, M. De Santo, and Th. Rasing, J. Appl. Phys. **93**, 6216 (2003).
[26] M. Fiebig, V. V. Pavlov, and R. V. Pisarev, J. Opt. Soc. Am. B **22**, 96 (2005).
[27] W. Kleemann and J. Dec, Phys. Rev. B **75**, 027101 (2007).
[28] S. A. Denev, T. T. A. Lummen, E. Barnes, A. Kumar, and V. Gopalan, J. Am. Ceram. Soc. **94**, 2699 (2011).
[29] Y. Uesu, H. Yokota, S. Kawado, J. Kaneshiro, S. Kurimura, and N. Kato, Appl. Phys. Lett. **91**, 182904 (2007).
[30] J. Kaneshiro, S. Kawado, H. Yokota, Y. Uesu, and T. Fukui, J. Appl. Phys. **104**, 054112 (2008).
[31] J. Kaneshiro, Y. Uesu, and T. Fukui, J. Opt. Soc. Amer. B **27**, 888 (2010).
[32] J. Kaneshiro and Y. Uesu, Phys. Rev. B **82**, 184116 (2010)
[33] SHG takes place when the symmetry of material is noncentrosymmetric, which can be nonpolar. It is known that the noncentrosymmetric point groups are classified into a polar group and a nonpolar group. Careful measurements and analyses of SHG can distinguish the sample belonging to the polar group or to the nonpolar group. It should be also noted that SH waves can be produced even in centrosymmetric crystals through a quadrupole and nonlinear magnetization. Under the nonresonance condition, which is the present case, the contribution from these effects can be estimated to have an order of a/λ. Here, a is a lattice constant and λ is the wavelength. Therefore, the contribution is 10^{-3} or even smaller than that of nonlinear polarization. Thus, we can safely neglect the quadrupole effect in the present experiments.
[34] M. Guennou, P. Bouvier, B. Krikler, J. Kreisel, R. Haumont, and G. Garbarino, Phys. Rev. B **82**, 134101 (2010).
[35] H. F. Kay and P. C. Bailey, Acta Crystallogr. **10**, 219 (1957).
[36] J. Sapriel, Phys. Rev. B **12**, 5128 (1975).
[37] K. Aizu, J. Phys. Soc. Jpn. **28**, 706 (1970).
[38] S. A. T. Redfern, J. Phys. Condens. Matter **8**, 8267 (1996).
[39] The inclinations of TBs calculated with the experimentally obtained strains and the refractive index are not perfectly coincident with the experimental results. The error of the strains e_{11} and e_{12}, would be small, estimated 1%, but the error of the

refractive index of CTO is large (10%) because the exact values of the refractive indices of CTO are not known. These errors together with the orientation error of 4 degree of the samples can explain the deviation of the calculation from the experiment.

[40] J. F. Nye, *Physical Properties of Crystals* (Oxford University Press, Oxford, UK, 1957).

[41] D. AKleinman, Phys. Rev. **126**, 1977 (1962).

[42] To determine the symmetry using SHG, we should adopt the symmetry that can be explained by the minimum number of adjustable parameters. In the present case, the lower symmetry of triclinic 1 is also allowed, but the number of adjustable parameters is much larger than the case of 2 and *m*. Judging from the symmetry of the polar diagram form in Figs. 5 and 6, the 2 or *m* symmetry is most plausible within the experimental error.

[43] A. N. Morozovska, E. A. Eliseev, M. D. Glinchuk, L-Q. Chen, and V. Gopalan, Phys. Rev. B **85**, 094107 (2012)

[44] A. M. Glazer, Acta Crystallogr. B **28**, 3384 (1972)